Biosensors and Bioelectronics 185 (2021) 113250

Contents lists available at ScienceDirect

Biosensors and Bioelectronics

journal homepage: http://www.elsevier.com/locate/bios

Engineering paper-based visible light-responsive Sn-self doped domed SnO_2 nanotubes for ultrasensitive photoelectrochemical sensor

Haihan Yu [a], Xiaoran Tan [a], Shubo Sun [b], Lina Zhang [b], Chaomin Gao [a,*], Shenguang Ge [c,**]

[a] School of Chemistry and Chemical Engineering, University of Jinan, Jinan, Shandong, 250022, PR China
[b] Shandong Provincial Key Laboratory of Preparation and Measurement of Building Materials, University of Jinan, Jinan, Shandong, 250022, PR China
[c] Institute for Advanced Interdisciplinary Research, University of Jinan, Jinan, 250022, PR China

ARTICLE INFO

Keywords:
Photoelectrochemical biosensor
Charge separation
SnO_2.x nanotubes

ABSTRACT

Exploring novel photoactive materials with high photoelectric conversion efficiency plays a crucial role in enhancing the analytical performance of paper-based photoelectrochemical (PEC) biosensor. SnO_2, which possesses higher photostability and electron mobility, can be regarded as a promising photoactive material. Herein, paper-based one dimensional (1D) domed SnO_2 nanotubes (NTs) have been developed with the template-consumption strategy. What's more, their growth mechanism has also been proposed based on the controllable experiments. At first, the paper-based 1D ZnO nanorods (NRs) as the typical amphoteric oxide are prepared and serve as the sacrifice templates which can be etched by the generated alkaline environment during the formation of SnO_2. At a certain stage, all the ZnO NRs can be completely etched by controlling the experimental conditions, resulting in the forming of vertically distributed hollow SnO_2 NTs. Furthermore, the Sn self-doping strategy is also proposed to suppress the recombination of charge carriers and broaden the light response range by introducing the impurity energy levels. Profiting from such doping strategy, the prominent photocurrent signal is obtained compared with pure paper-based SnO_2 NTs. Ultimately, an innovative visible light responsive paper-based Sn-doping SnO_{2-x} NTs are developed and employed as the photoelectrode for the PEC biosensor using the alpha fetoprotein (AFP) as the model analyte. Under the optimal conditions, the ultrasensitive AFP sensing is realized with the linear range and detection limitation of 10 pg mL^{-1} to 200 ng mL^{-1} and 3.84 pg mL^{-1}, respectively. This work provides a judiciously strategy for developing novel photoactive materials for paper-based PEC bioanalysis.

1. Introduction

Cellulose paper, as a great innovation of ancient China, has been extensively applied in our daily life for being a considerable material for writing, printing and decoration (Nery and Kubota, 2013; Uematsu et al., 2011). Meanwhile, featuring with the merits of lowcost, great biocompatibility and modifiable character, cellulose paper has also been extensively investigated in the biological analysis field (Martinez et al., 2010; Pelton, 2009). Ever since the concept of patterned paper was proposed by Whitesides to construct sensing platform (Martinez et al., 2007), paper-based analytical devices have attracted considerable attention (Nery and Kubota, 2013; Scala-Benuzzi et al., 2018; Schaumburg et al., 2019). Among them, by virtue of high sensitivity, portability and cost-effective feature, paper-based photoelectrochemical (PEC) biosensors have gained much interest (Gao et al., 2018a). Since the photocurrent is utilized as the detection signal, the analytical performance of paper-based PEC biosensor depends heavily on the photoelectric conversion properties of the employed photoactive materials (Gao et al., 2018b; Zhao et al., 2014). Hence, the photoactive materials and their charge separation efficiency are crucial for achieving high sensitivity (Josset et al., 2008; Kwon et al., 2014). To date, various nanomaterials, mainly metal oxide semiconductors, have been explored in paper-based PEC biosensors (Gao et al., 2019; Song et al., 2018; Wang et al., 2020b). Among them, SnO_2, as a n-type semiconductor, has been regarded as a promising one ascribing to the following advantages: (1) the high electron mobility (240 cm^2 V^{-1} s^{-1}) (Xiong et al., 2018) can potentially enhance the efficiency of electronic transmission and reduce the recombination rate of electron-hole pairs (Ke et al., 2015; Ren et al.,

* Corresponding author.
** Corresponding author.
E-mail addresses: chm_gaocm@163.com (C. Gao), chm_gesg@163.com (S. Ge).

https://doi.org/10.1016/j.bios.2021.113250
Received 2 February 2021; Received in revised form 7 April 2021; Accepted 10 April 2021
Available online 15 April 2021
0956-5663/© 2021 Elsevier B.V. All rights reserved.

2017; Xiong et al., 2016); (2) Compared with TiO_2 and ZnO, SnO_2 possesses higher photostability under UV light irradiation (Tiwana et al., 2011; Zhang et al., 2018); (3) The crystallization temperature of SnO_2 is below than that of TiO_2, making it easier to crystallize as well as doping (Ren et al., 2017). In particular, benefiting from the enlarged surface area to volume ratio, higher light absorption efficiency and reduced lateral charge migration distance, one dimensional (1D) nanostructure SnO_2 has aroused tremendous interest in the field of photovoltaic conversion (Fan et al., 2018; Han et al., 2018; Luo et al., 2020; Yang et al., 2017). Nevertheless, the growth of 1D SnO_2 nanorods (NRs) or nanotubes (NTs) on a given substrate still remains a challenge. Generally, the SnO_2 NTs were usually prepared using the two-step template-assisted method, which requires the time-consuming acid etching step. Most importantly, engineering paper-based 1D SnO_2 NTs has not been reported and utilized in PEC bioanalysis. Herein, aiming to construct a low-cost and high-performance paper-based PEC biosensor, paper-based SnO_2 NTs arrays are prepared for the first time based on the template-consumption strategy with the ZnO NRs acting as the templates and without any acid etching step.

Despite with excellent photostability, the large bandgap and high charge carrier recombination rate limit the application of SnO_2 in visible-light driven PEC biosensor (Yang et al., 2021; Tang et al., 2013; Wang et al., 2016). Therefore, facilitating the efficient carriers separation and broadening its light absorption range are of great significance towards ultrasensitive PEC biosensor. Up to date, various strategies have been developed to achieve these goals (Shu and Tang, 2020). Among them, element doping receives extensive concern because it can not only widen the light absorption region but also suppress the recombination of photo-induced charge carriers (Teoh et al., 2012; Wang et al., 2020a). Thereinto, self-doping strategy, unlike doping with foreign elements, can better minimize the structural defects due to the small distinction in ion size between the host and dopant ions, and thus decrease the recombination center of charge carriers (Fan et al., 2013; Lin et al., 2017). Therefore, the Sn self-doping strategy was adopted to facilitate the separation of charge carriers and broaden the absorption range to visible region by introduction the impurity energy levels in the SnO_2 NTs.

In this work, 1D SnO_2 NTs grown on the cellulose paper though a facile but valid in-situ template-consumption strategy using ZnO NRs as the templates were successfully demonstrated. Their growth mechanism was also investigated with the controlled experiments. Furthermore, in order to promote the efficient charge carrier separation and broaden the light response range to visible region, the Sn self-doping strategy was also proposed. Finally, the model analyte of alpha fetoprotein (AFP) was selected to investigated the application of as-prepared photoelectrode in visible-driven paper-based PEC biosensor.

2. Experimental section

2.1. Preparation of paper-based ZnO nanorods (NRs)

Firstly, the Au NPs layer was modified onto the paper working zone to endow the great conductivity. Briefly, the Au NPs seeds solution, which contains 0.2 mM chloroauric acid and 0.9 mM trisodium citrate, was firstly dripped onto the working zone, followed by drying in ambient air at room temperature. After repeating the above steps for 5 times, the growth solution (1 mL) prepared by mixing 200 mM hydroxylammonium chloride solution (0.5 mL) with 20 mM chloroauric acid solution (0.5 mL) was added to the working zone and incubated for 10 min at room temperature. After that, the working zone was washed with ultrapure water and dried at room temperature.

A perpendicular ZnO NRs arrays, which acted as sacrificial templates, were firstly obtained through seeds-assisted approach. Briefly, the zinc acetate (50 mM) solution was modified onto the surface of paper with spin-coating method, serving as the seed layers. Then, 56.9 mg zinc acetate and 42.1 mg hexamethylenetetramine were dissolved in 20 mL ultrapure water under continuous stirring. The obtained solution was then shifted to the Teflon-lined stainless-steel autoclave, in which the ZnO seeds/paper was placed. Subsequently, the autoclave was hydrothermally treated in a dry oven at 95 °C for 3 h. After cooling to room temperature, the paper-based ZnO NRs were taken out and washed with ultrapure water for 3 times, followed by drying at 60 °C in a dry oven.

2.2. Preparation of paper-based SnO_2 nanotubes (NTs)

Initially, 6.0 mM sodium stannate and 4.0 mM urea were added into 15 mL mixture of ethanol and ultrapure water, followed by vigorous stirring. After that, the as-prepared paper-based ZnO NRs were put into the Teflon-lined stainless-steel autoclave, followed by adding the above suspension into the autoclave. Then the autoclave was hydrothermally treated at temperature of 170 °C for 110 min. Finally, the obtained sample was washed thoroughly with ultrapure water and dried at 60 °C.

2.3. Preparation of Sn doped paper-based SnO_2 NTs

Typically, 5.8 mM $SnCl_4{\cdot}5H_2O$ was dissolved in 40 mL water, followed by addition of 2.9 mM Sn powder under continuously stirring for 1 h. The obtained solution and the SnO_2 NTs were transferred to the autoclave and heated in a dry oven at 120 °C for 4 h. After cooling to room temperature in ambient air, the sample was taken out and washed using ultrapure water for 3 times. Finally, the paper-based Sn doped SnO_{2-x} NTs array was dried at 60 °C in a dry oven.

2.4. Design of the paper-based PEC sensor

Since the growth temperature of SnO_2 is higher than the melting temperature of wax, the hand-painted wax method was adopted. After modification with the material, the paper was hand-painted with wax and heated to let the waxes melt and permeate through the paper to construct valid hydrophobic barriers. Subsequently, carbon and Ag/AgCl, which acted as the counter electrode and the reference electrode, respectively, were printed using the screen-printing strategy. The shape patterns of the hydrophobic region and the photographs of the paper-based PEC sensor were designed using Adobe CS6 as shown in the Supporting Information (Fig. S1 and Fig. S2).

3. Results and discussion

3.1. Preparation of as-constructed PEC sensor and characterization of obtained samples

The preparation of paper-based PEC sensor and its assay procedures were shown in Scheme 1. Firstly, the vertical distribution of ZnO NRs were obtained with the hydrothermal method onto the working zone. Then the template-consumption strategy and doping method were employed to growth the SnO_2 NTs and Sn doped SnO_{2-x} samples. After that, 20 μL of 0.1 wt % chitosan solution was dropped onto the working zone and left to dry in ambient air at room temperature, followed by washing thoroughly using 0.1 M NaOH and ultrapure water. The photoelectrode was then activated by 25 μL of 5 wt % glutaraldehyde solution for 30 min. After that, the sample was washed with ultrapure water and dried at room temperature. Subsequently, 25 μL AFP antibody solution was added onto the photoelectrode and incubated for 6 h, followed by washing with ultrapure water for 3 times. Finally, the non-specific binding sites were blocked by 25 μL phosphate buffer saline (PBS) solution (0.1 M, pH 7.4) containing 0.25% bovine serum albumin (BSA), and the photoelectrode was then washed with PBS (0.1 M, pH 7.4) solution to remove uncombined biomolecules. The assay procedures were shown in the Supporting Information.

The morphologies of obtained samples were first characterized using scanning electron microscope (SEM). It can be seen from the Fig. 1a, countless cellulose fibers interweaved with each other to construct a

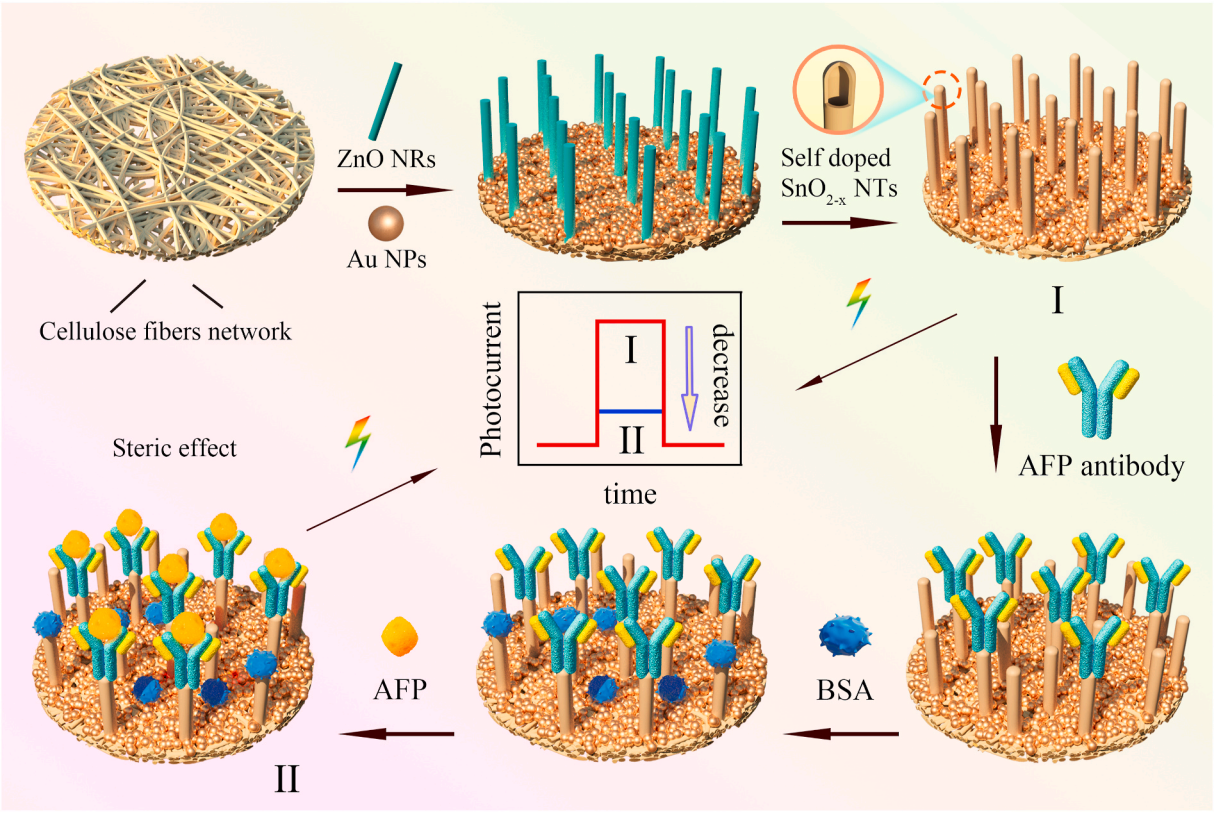

Scheme 1. The construction of paper-based Sn doped SnO_{2-x} sample and assay procedures of the as-constructed PEC sensor.

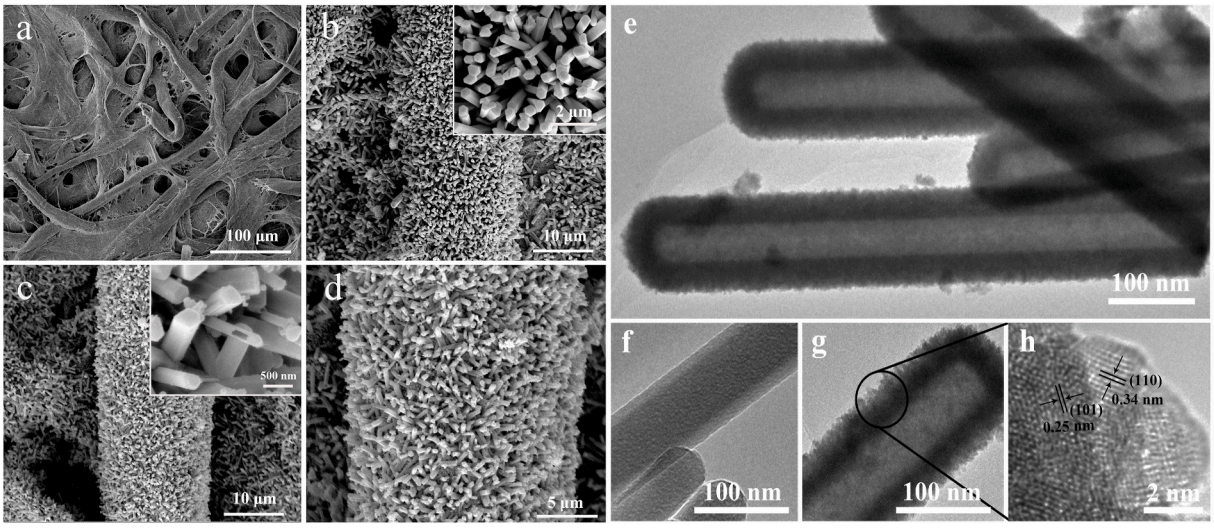

Fig. 1. (a) The SEM image of pure paper, (b) paper-based ZnO NRs, (c) SnO_2 NTs (d) and Sn doped SnO_{2-x} NTs, (e) TEM images of paper-based SnO_2 NTs, (f) ZnO NRs and (g) Sn-doped SnO_{2-x} NTs. (h) High-resolution TEM image of paper-based SnO_{2-x} NTs. Insets in Fig. b and c were high magnification SEM image of paper-based ZnO NRs and SnO_2 NTs, respectively.

porous network, offering abundant active sites. After the hydrothermal reaction, the ZnO NRs resulted to be orderly and densely aligned in vertical standing format, covering the entire surface of cellulose fibers (Fig. 1b). As shown in the high magnification SEM image (Inset of Fig. 1b), the ZnO NRs with smooth surfaces were grown uniformly and their diameters were approximately 300 nm. Most importantly, after the template-consumption growth processes, the vertically oriented SnO_2 were decorated onto the fibers (Fig. 1c). Observed at high magnification SEM image, the obtained SnO_2 exhibited a hollow NT configuration with an increased diameter (inset of Fig. 1c). After doping with Sn powder, no distinct change of morphology was observed and the tubular structure was remained, as shown in Fig. 1d.

Transmission electron microscope (TEM) was also carried out to investigate the microstructure of as-prepared samples. As shown in Fig. 1f, the paper-based ZnO showed a typical solid NR structure. After the hydrothermal reaction, ZnO NRs core disappeared owing to the etching effect and the obtained SnO_2 exhibited a tubular structure, of which the shell thickness was around 30 nm (Fig. 1e). In addition, the

NT structure was remained after the doping process as shown in Fig. 1g. Moreover, the lattice fingers of the self-doped SnO_{2-x} shell with spacing of 0.34 nm and 0.25 nm were ascribed to the (110) and (101) crystal faces of rutile SnO_2, respectively (Fig. 1h).

To further study the crystallinity of obtained samples, X-ray diffraction (XRD) characterization was also performed. As shown in Fig. S3a, the characteristic peaks of tetragonal SnO_2 at (110), (101) and (211) planes could be observed (JCPDS card No. 46-1088), indicating the successful preparation of paper-based SnO_2 NTs. After doping with Sn powder, no evident changes of the diffraction peaks were observed and no other phases were detected. Moreover, X-ray photoelectron spectroscopy (XPS) characterization was also implemented to verify their elements and valence state. As shown in Fig. S3b, the samples consisted of Sn, C and O elements, no impurity elements were observed, further manifesting the high purity. Meanwhile, as shown in high-resolution XPS spectra of Sn 3d (Fig. 2a), the two peaks approximately centered at 487.5 eV and 495.9 eV with a spin-orbit splitting energy of 8.4 eV which belonged to $3d_{5/2}$ and Sn $3d_{3/2}$, respectively, were in accordance with the Sn^{4+} peaks (Dong et al., 2017; Wang et al., 2012b; Yang et al., 2013). However, after doping, the binding energy of Sn in SnO_{2-x} decreased by 0.2 eV compared to that of pure SnO_2 (Fig. S3c), ascribing to the presence of oxygen vacancies generated by the doping possess (Han et al., 2017; Wang et al., 2013). Meantime, the signals of Sn can be deconvoluted into Sn^{4+} and Sn^{2+} signals (Fig. 2b), verifying the presence of Sn^{2+} dopants in paper-based SnO_{2-x} NTs. The about 0.7 eV binding energy shift between Sn^{4+} and Sn^{2+} was in agreement with previous reports (Wang et al., 2012a; Zhu et al., 2015). Besides, the O 1s high-resolution XPS spectra of self-doped SnO_{2-x} NTs was shown in Fig. 2c. The peak located at 531.1 eV was attribute to the coordinating oxygen bonded to Sn (O_L), while the higher binding energy was associated with the oxygen vacancies (O_V) formed to preserve the electric neutrality (Han et al., 2017; Zhu et al., 2015).

3.2. Growth mechanism of the paper-based SnO_2 NTs

Importantly, the growth mechanism of the paper-based SnO_2 NTs was investigated by measuring TEM images with different growth time. As shown in Fig. S4a, the pure ZnO NRs exhibited a rod-like structure. When the hydrothermal reaction time was 45 min, an incompact SnO_2 shell was observed on the surface of ZnO NRs due to the reaction of sodium stannate and urea (Fig. S4b). As shown in Fig. S4c, when the growth time increased to 75 min, a tubular structure with a dense shell was formed, implying the consumption of ZnO NRs sacrificial templates. Besides, a calotte-like cap cloud be observed at the top of the SnO_2 NTs, which was in accordance with SEM observation. Finally, when the reaction time was prolonged to 105 min, a denser and thicker SnO_2 shell was observed, no evident residual ZnO was detected (Fig. S4d), indicating that the ZnO NRs core were etched off thoroughly by the produced OH^-.

Based on the above experiment results, the possible growth mechanism was predicted, as shown in Scheme 2. Specifically, under the hydrothermal condition, the urea began to hydrolyze and carbon dioxide (CO_2) as well as ammonia (NH_3) were produced (eq (1)). The sodium stannate can react with the generated CO_2 and formed SnO_2 crystals through reaction eq (2) (Juttukonda et al., 2006). The formed NH_3 can lead to an alkaline environment (eq (3)) which can dissolve the typical amphoteric oxide of ZnO (eq (4)) (She et al., 2008). As a consequence, the ZnO NRs templates can be in-situ etched off and the SnO_2 NTs were obtained through controlling the reaction time.

$$CO(NH_2)_2 + H_2O \rightarrow CO_2 + NH_3 \quad (1)$$

$$Na_2SnO_3 + CO_2 \rightarrow SnO_2 + Na_2CO_3 \quad (2)$$

$$NH_3 + H_2O \rightarrow NH_4^+ + OH^- \quad (3)$$

$$ZnO + OH^- \rightarrow ZnO^{2-} + H_2O \quad (4)$$

3.3. Characterization of photoelectric properties of paper-based SnO_2 NTs and SnO_{2-x} NTs

In order to evaluate the promoting effect of Sn doping on light absorption performance, UV–vis spectra of the samples prepared on FTO/glass with the same method were measured. As shown in Fig. 3a, the pure SnO_2 exhibited a light absorption edge at wavelength about 380 nm, while that of SnO_{2-x} had been shifted to around 500 nm, indicating that the Sn self-doping strategy can efficiently extend the absorption range to the visible region. Furthermore, the photocurrent responses of paper-based SnO_2 NTs and SnO_{2-x} NTs under visible light illumination were also investigated. As shown in Fig. 3b, paper-based Sn-doped SnO_{2-x} exhibited obvious photocurrent, whereas SnO_2 NTs showed almost no photocurrent response, further demonstrating that Sn doping can effectively enhance the photocurrent response of SnO_2 under visible light radiation.

What's more, to reveal the promotion of Sn doping on the separation efficiency of electron-hole pairs, steady state photoluminescence (PL) and time-resolved photoluminescence (TRPL) spectra were measured with the excitation source of 340 nm wavelength. As shown in Fig. 3c, the paper-based SnO_2 NTs exhibited a strong PL signal owing to the relatively high recombination rate of photogenerated charge carriers. After doping, a dramatic decreased PL signal was observed, suggesting that the Sn doping can efficiently suppress the recombination of carriers. In addition, the TRPL spectra was also performed to investigate the transfer dynamics of photo-induced carriers (Fig. 3d). The exponential decay model fit curves for both paper-based SnO_2 and SnO_{2-x} were obtained and their fitted parameters were shown in Table S1. As for the

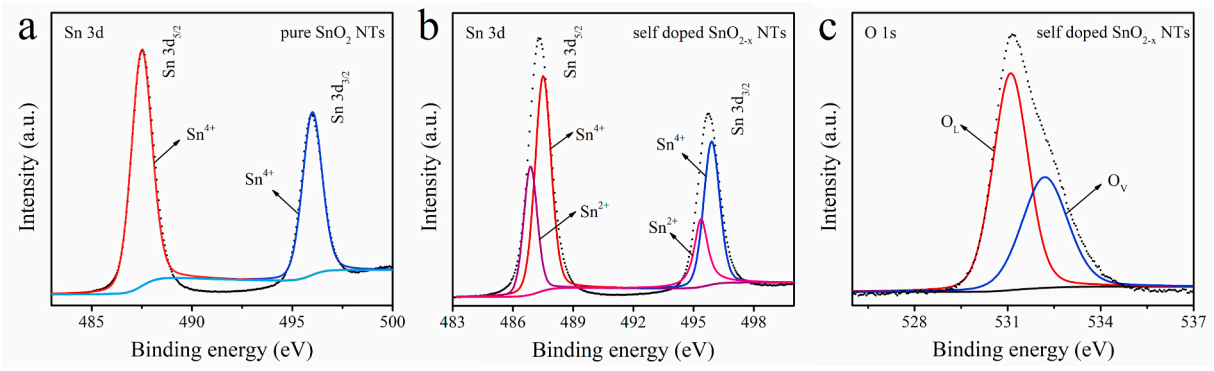

Fig. 2. (a) High-resolution XPS spectra of Sn 3d orbitals of paper-based SnO_2 NTs and (b) paper-based self-doped SnO_{2-x} NTs .(c) O 1s orbital of paper-based self-doped SnO_{2-x} NTs.

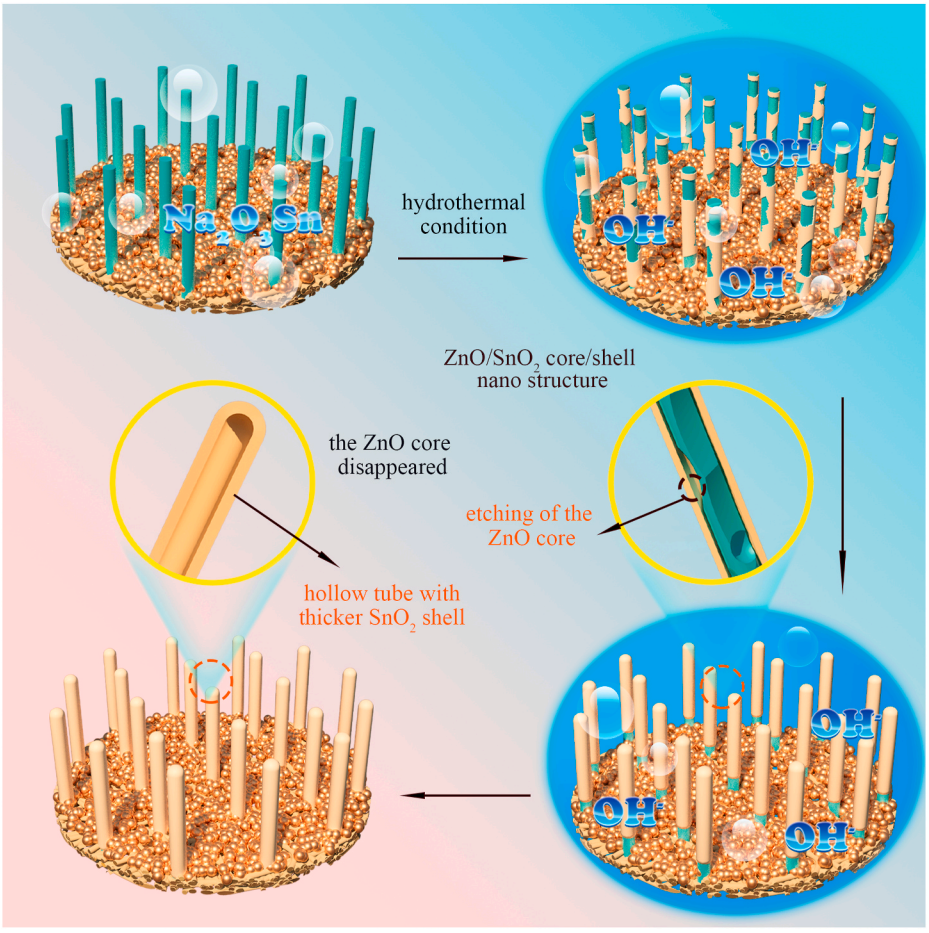

Scheme 2. The schematic diagram of formation processes of paper-based SnO_{2-x} NTs based on the template-consumption strategy.

pure paper-based SnO_2, a high carrier lifetime of 15.43 ns was observed. After Sn doped, the lifetime was reduced to 5.18 ns, implying that Sn self-doping strategy can greatly improve the carrier separation efficiency (Gao et al., 2020).

3.4. Analytical performance

Under the optimal conditions, the analytical performance of as-constructed paper-based PEC sensor for AFP detection was evaluated. Fig. 4a exhibited the photocurrent responses of the sensor with various concentrations of AFP. As the concentration of AFP increased, a large amount of target immune molecules was captured specifically though the recognition layer on the photoelectrode, which gave rise to the steric effect and thus caused the gradually decrease of photocurrent intensity. In addition, the calibration curve under optimum experimental conditions was shown in Fig. 4b. The linear equation was $I = 8.17\text{-}2.61 \log c$, with a correlation coefficient of 0.997 and a linear range from 10 pg mL^{-1} to 200 ng/mL. What's more, the detection limit was as low as 3.84 pg/mL (based on a signal-to-noise ratio of 3) (Gong et al., 2016; Tiwari et al., 2016; Zhu et al., 2020), attributing to the superior photoelectric conversion performance of SnO_2 and the Sn self-doping strategy. Compared with previously reports, the as-designed PEC sensor possessed lower detection limit (Table S2). In addition, the analytical experimental conditions of PEC sensor were also optimized as shown in Fig. S5.

3.5. Feasibility, reproducibility, specificity and stability of the paper-based PEC sensor

The feasibility was evaluated with the standard addition method, as shown in Table S3. The recovery was from 94.4% to 107.8%, implying the great application potential of constructed paper-based PEC sensor. Furthermore, the reproducibility was assessed though the interassay precision of ten independent devices. The RSDs of parallel detection of 0.1, 10 and 100 ng/mL AFP with ten sensors were 2.93%, 3.22% and 3.89%, respectively, suggesting the acceptable reproducibility. In addition, the prostate specific antigen (PSA), carcinoembryonic antigen (CEA), human serum albumin (HSA) and hemoglobin (Hb) were selected as interfering agents to evaluate the specificity. As shown in Fig. 4c, only the AFP can result in an obvious photocurrent decreasing, demonstrating the satisfying selectivity. The stability was also investigated by measuring the time-based photocurrent response under optimum experimental conditions (Fig. 4d). As seen, no obvious change of the photocurrent intensity was observed with on/off visible light irradiation cycles for 1000 s, certifying the high photostability of the constructed sensor.

4. Conclusion

In this work, the novel paper-based 1D SnO_2 NTs were prepared based on the template-consumption strategy and served as the photoactive material for the first time. The growth mechanism was also proposed with the controllable experiments. Furthermore, Sn self-doping method was proposed to facilitate the separation of photo-induced charge carriers and enhance the visible light harvesting. Besides, self-doping of Sn can narrow the band gap of SnO_2 NTs and reduce the recombination rate of charge carriers, which resulted in a considerable enhancement of photocurrent intensity under visible light illumination. Based on such desired detection signal, the as-designed paper-based PEC

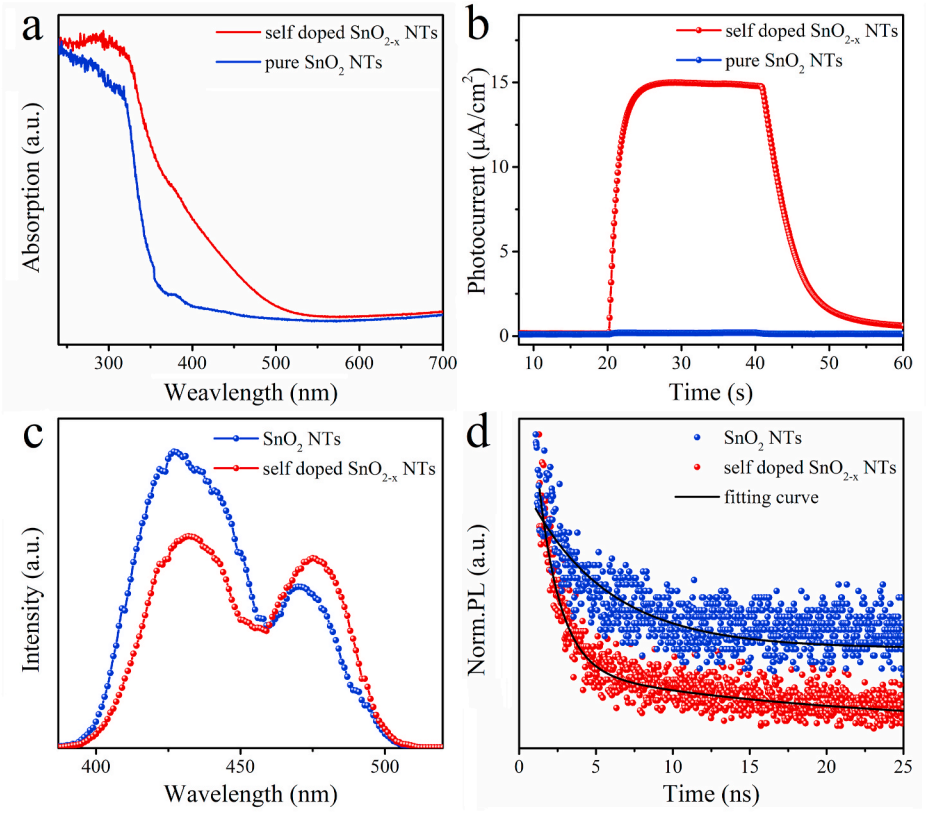

Fig. 3. (a) UV–vis spectra of the samples prepared on FTO/glass using the same method and (b) photocurrent response of samples under visible light illumination. (c) PL and (d) TRPL spectra of paper-based SnO_2 NTs and Sn doped SnO_{2-x} NTs.

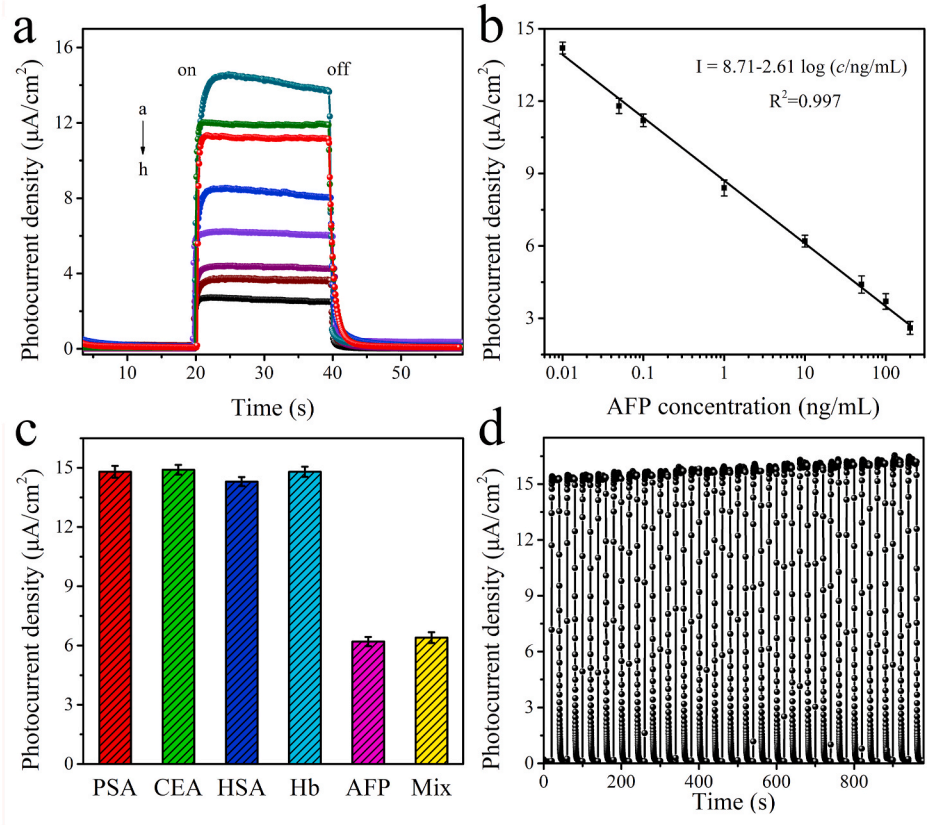

Fig. 4. (a) Photocurrent density of the constructed paper-based PEC sensor incubated with various AFP concentration (a–h: 0.01, 0.05, 0.1, 1, 10, 50, 100, 200 ng/mL). (b) The linear calibration curve of the constructed sensor. (c) The specificity and (d) stability of the proposed paper-based PEC sensor.

biosensor demonstrated the ultrasensitive sensing of AFP.

CRediT authorship contribution statement

Haihan Yu: Conceptualization, Methodology, Writing – original draft. **Xiaoran Tan:** Investigation, Formal analysis. **Shubo Sun:** Visualization, Data curation. **Lina Zhang:** Resources, Visualization. **Chaomin Gao:** Writing – review & editing, Resources. **Shenguang Ge:** Supervision, Funding acquisition, Project administration.

Declaration of competing interest

The authors declare that they have no known competing financial interests or personal relationships that could have appeared to influence the work reported in this paper.

Acknowledgements

This work was financially supported by the National Natural Science Foundation of China (21874055, 51872121, 22074053, 21775055), the Taishan Scholars Program, the Case-by-Case Project for Top Outstanding Talents of Jinan, and the project of "20 items of University" of Jinan (2018GXRC001), Excellent Youth Innovation Team in Universities of Shandong (2019KJC016).

Appendix A. Supplementary data

Supplementary data to this article can be found online at https://doi.org/10.1016/j.bios.2021.113250.

References

Dong, W.J., Xu, J.J., Wang, C., Lu, Y., Liu, X.Y., Wang, X., Yuan, X.T., Wang, Z., Lin, T.Q., Sui, M.L., Chen, I.W., Huang, F.Q., 2017. Adv. Mater. 29, 1700136.
Fan, C.M., Peng, Y., Zhu, Q., Lin, L., Wang, R.X., Xu, A.W., 2013. J. Phys. Chem. C 117, 24157–24166.
Fan, L., Xia, Z., Xu, M.J., Lu, Y.Y., Li, Z.J., 2018. Adv. Funct. Mater. 28, 1706289.
Gao, C.M., Xue, J., Zhang, L.N., Cui, K., Li, H., Yu, J.H., 2018a. Anal. Chem. 90, 14116–14120.
Gao, C.M., Xue, J., Zhang, L.N., Zhao, P.N., Cui, K., Ge, S.G., Yu, J.H., 2019. Biosens. Bioelectron. 131, 17–23.
Gao, C.M., Yu, H.H., Zhang, L.N., Zhao, Y.H., Xie, J., Li, C.J., Cui, K., Yu, J.H., 2020. Anal. Chem. 92, 2902–2906.
Gao, Y., Wang, J.L., Mo, S.Y., Wang, F.W., Long, F., Zou, Z.G., 2018b. Solar. RRL. 2, 1800015.
Gong, L., Dai, H., Zhang, S., Lin, Y., 2016. Anal. Chem. 88, 5775–5782.
Han, D., Jiang, B., Feng, J., Yin, Y., Wang, W., 2017. Angew. Chem. Int. Ed. 56, 7792–7796.
Han, H., Kment, S., Karlicky, F., Wang, L., Naldoni, A., Schmuki, P., Zboril, R., 2018. Small 14, 1703860.
Josset, S., Keller, N., Lett, M.C., Ledoux, M.J., Keller, V., 2008. Chem. Soc. Rev. 37, 744–755.
Juttukonda, V., Paddock, R.L., Raymond, J.E., Denomme, D., Richardson, A.E., Slusher, L.E., Fahlman, B.D., 2006. J. Am. Chem. Soc. 128, 420–421.
Ke, W., Fang, G., Liu, Q., Xiong, L., Qin, P., Tao, H., Wang, J., Lei, H., Li, B., Wan, J., Yang, G., Yan, Y., 2015. J. Am. Chem. Soc. 137, 6730–6733.
Kwon, W., Lee, G., Do, S., Joo, T., Rhee, S.W., 2014. Small 10, 506–513.
Lin, Y., Zhou, Q., Tang, D., 2017. Anal. Chem. 89, 11803–11810.
Luo, J., Jiang, Y.N., Guo, X.Y., Ying, Y., Wen, Y., Lin, P., Sun, Y., Yang, H.F., Wu, Y.P., 2020. Sensor. Actuator. B Chem. 309, 127714.
Martinez, A.W., Phillips, S.T., Butte, M.J., Whitesides, G.M., 2007. Angew. Chem. Int. Ed. 119, 1340–1342.
Martinez, A.W., Phillips, S.T., Whitesides, G.M., Carrilho, E., 2010. Anal. Chem. 82, 3–10.
Nery, E.W., Kubota, L.T., 2013. Anal. Bioanal. Chem. 405, 7573–7595.
Pelton, R., 2009. Trends Anal. Chem. 28, 925–942.
Ren, X., Yang, D., Yang, Z., Feng, J., Zhu, X., Niu, J., Liu, Y., Zhao, W., Liu, S.F., 2017. ACS Appl. Mater. Interfaces 9, 2421–2429.
Scala-Benuzzi, M.L., Raba, J., Soler-Illia, G., Schneider, R.J., Messina, G.A., 2018. Anal. Chem. 90, 4104–4111.
Schaumburg, F., Carrell, C.S., Henry, C.S., 2019. Anal. Chem. 91, 9623–9630.
She, G.W., Zhang, X.H., Shi, W.S., Fan, X., Chang, J.C., Lee, C.S., Lee, S.T., Liu, C.H., 2008. Appl. Phys. Lett. 92, 053111.
Shu, J., Tang, D., 2020. Anal. Chem. 92, 363–377.
Song, Z., Fan, G.C., Li, Z., Gao, F., Luo, X., 2018. Anal. Chem. 90, 10681–10687.
Tang, Y., Di, W., Zhai, X., Yang, R., Qin, W., 2013. ACS Catal. 3, 405–412.
Teoh, W.Y., Scott, J.A., Amal, R., 2012. J. Phys. Chem. Lett. 3, 629–639.
Tiwana, P., Docampo, P., Johnston, M.B., Snaith, H.J., Herz, L.M., 2011. ACS Nano 5, 5158–5166.
Tiwari, J.N., Vij, V., Kemp, K.C., Kim, K.S., 2016. ACS Nano 10, 46–80.
Uematsu, T., Matsui, Y., Kakiuchi, S., Isogai, A., 2011. Cellulose 18, 1129–1138.
Wang, C., Du, G., Ståhl, K., Huang, H., Zhong, Y., Jiang, J.Z., 2012a. J. Phys. Chem. C 116, 4000–4011.
Wang, H., Dou, K., Teoh, W.Y., Zhan, Y., Hung, T.F., Zhang, F., Xu, J., Zhang, R., Rogach, A.L., 2013. Adv. Funct. Mater. 23, 4847–4853.
Wang, J.P., Li, D.B., Xu, C.H., Yuan, X.M., Yang, P., 2020a. Superlattice. Microst. 138, 106387.
Wang, K.W., Zhang, R.H., Sun, N., Li, X.P., Wang, J.N., Cao, Y., Pei, R.J., 2016. ACS Appl. Mater. Interfaces 8, 25834–25839.
Wang, S.P., Wang, F.F., Fu, C.P., Sun, Y.N., Zhao, J.G., Li, N., Liu, Y.Q., Ge, S.G., Yu, J.H., 2020b. Anal. Chem. 92, 7604–7611.
Wang, X., Cao, X.Q., Bourgeois, L., Guan, H., Chen, S.M., Zhong, Y.T., Tang, D.M., Li, H. Q., Zhai, T.Y., Li, L., Bando, Y., Golberg, D., 2012b. Adv. Funct. Mater. 22, 2682–2690.
Xiong, L., Qin, M.C., Chen, C., Wen, J., Yang, G., Guo, Y.X., Ma, J.J., Zhang, Q., Qin, P.L., Li, S.Z., Fang, G.J., 2018. Adv. Funct. Mater. 28, 1706276.
Xiong, L.B., Qin, M.C., Yang, G., Guo, Y.X., Lei, H.W., Liu, Q., Ke, W.J., Tao, H., Qin, P.L., Li, S.Z., Yu, H.Q., Fang, G.J., 2016. J. Mater. Chem. A. 4, 8374–8383.
Yang, F., Yang, F., Tu, T.T., Liao, N., Chai, Y.Q., Yuan, R., Zhuo, Y., 2021. Biosens. Bioelectron. 173, 112820.
Yang, S., Yue, W.B., Zhu, J., Ren, Y., Yang, X.J., 2013. Adv. Funct. Mater. 23, 3570–3576.
Yang, Z., Wang, H., Song, W., Wei, W., Mu, Q., Kong, B., Li, P., Yin, H., 2017. J. Colloid Interface Sci. 486, 232–240.
Zhang, P., Wu, J., Zhang, T., Wang, Y., Liu, D., Chen, H., Ji, L., Liu, C., Ahmad, W., Chen, Z.D., Li, S., 2018. Adv. Mater. 30, 1703737.
Zhao, W.W., Xu, J.J., Chen, H.Y., 2014. Chem. Rev. 114, 7421–7441.
Zhu, P.H., Li, S.S., Zhao, C.R., Zhang, Y., Yu, J.H., 2020. J. Hazard Mater. 384, 121426.
Zhu, Y.Q., Guo, H.Z., Zhai, H.Z., Cao, C.B., 2015. ACS Appl. Mater. Interfaces 7, 2745–2753.